ADVANCED FUNCTIONAL MATERIALS
www.afm-journal.de

# Field-Induced Butterfly-Like Anisotropic Magnetoresistance in a Kagome Semimetal $Co_3In_2S_2$

*Senhao Lv, Hui Guo, Qi Qi, Yuhui Li, Guojing Hu, Qi Zheng, Ruwen Wang, Nan Si, Ke Zhu, Zhen Zhao, Yechao Han, Weiqi Yu, Guoyu Xian, Li Huang, Lihong Bao, Xiao Lin, Jinbo Pan, Shixuan Du, Jun He,* Haitao Yang,* and Hong-Jun Gao*

**With the interplay between magnetism and topological bands, magnetic kagome semimetals provide promising platforms for exploring exotic correlated electronic states and quantum phenomena such as anomalous Hall effect, quantum spin liquid, and unconventional magnetoresistance, as well as driving advances in electronic and spintronic applications. Here, a field-induced butterfly-like anomalous anisotropic magnetoresistance (AMR) effect in an intriguing kagome semimetal $Co_3In_2S_2$ is reported. The kagome-lattice $Co_3In_2S_2$ single crystals are synthesized via a polycrystal-source chemical vapor transport approach, possessing a high carrier mobility reaching $10^4$ $cm^2V^{-1}s^{-1}$. The $Co_3In_2S_2$ single crystal exhibits a canted antiferromagnetic state below 5 K, but intriguingly, it is easily transformed into a ferromagnetic state under a small external magnetic field. Furthermore, the planar Hall effect (PHE) is detected, stemming from the complex contribution of field-induced ferromagnetism and orbital magnetoresistance. Remarkably, as the magnetic field increases, the low-temperature magnetoresistance behavior of the $Co_3In_2S_2$ reveals a butterfly-like AMR effect with a maximum value of 850%, exhibiting a superposition of the two-, four-, and six-fold AMR terms. Band structure calculations suggest that such a field-induced butterfly-like AMR effect may originate from the modulations of the electronic structure near the Fermi level by the magnetic moment. The findings offer a valuable platform for understanding the anomalous AMR effect and for the development of advanced spintronic devices.**

## 1. Introduction

Kagome-lattice materials, composed of corner-sharing triangles with a strong geometric frustration effect, have recently become a frontier in condensed matter systems.[1–3] Due to the presence of multiple spin, charge, and orbit degrees of freedom, along with nontrivial electronic structures such as flat bands, van Hove singularities, and Dirac points, kagome lattice materials provide a rich playground for studying the emergent quantum states, electronic orders and their correlations.[4–8] An emerging category of the kagome lattice materials is the magnetic kagome semimetals, which have revealed rich exotic properties such as Berry curvature-induced large anomalous Hall effect (AHE), spin-orbit polaron, chiral anomaly, high anomalous Nernst signal, and quantum AHE predicted in the 2D limit.[9–15] Particularly in the case of the antiferromagnetic Heisenberg model on a triangle sublattice, the kagome lattice is also expected to be one of the candidates to realize noncollinear/noncoplanar spin-frustrated antiferromagnetic states or even the quantum spin liquid.[16] Such noncollinear antiferromagnetic

S. Lv, J. He
Division of Functional Material Research
Central Iron & Steel Research Institute
Beijing 100081, P. R. China
E-mail: hejun@cisri.com.cn

S. Lv, H. Guo, Q. Qi, Y. Li, G. Hu, R. Wang, K. Zhu, Z. Zhao, Y. Han, W. Yu, G. Xian, L. Huang, L. Bao, J. Pan, S. Du, H. Yang, H.-J. Gao
Beijing National Center for Condensed Matter Physics and Institute of Physics
Chinese Academy of Sciences
Beijing 100190, P. R. China
E-mail: htyang@iphy.ac.cn

H. Guo, Q. Qi, G. Hu, Q. Zheng, R. Wang, K. Zhu, Z. Zhao, Y. Han, G. Xian, L. Huang, L. Bao, X. Lin, J. Pan, S. Du, H. Yang, H.-J. Gao
School of Physical Sciences
University of Chinese Academy of Sciences
Beijing 100049, PR China

N. Si
Multidisciplinary Center for Infrastructure Engineering
Shenyang University of Technology
Shenyang, Liaoning 110870, P. R. China

H. Yang, H.-J. Gao
Songshan Lake Materials Laboratory
Dongguan 523808, P. R. China

The ORCID identification number(s) for the author(s) of this article can be found under https://doi.org/10.1002/adfm.202412876

**DOI: 10.1002/adfm.202412876**

 

kagome semimetals exhibit unique intriguing phenomena under the external magnetic fields due to the spin-frustration-induced magnetic tunability,[17] providing more possibilities for practical device applications related to the spintronics.

In the development of spintronics, the research of the magnetoresistance effect in magnetic materials plays a significant role.[18,19] Especially, the anisotropic magnetoresistance (AMR) effect, which is defined as magnetoresistance changes with an angle between magnetization and current, becomes an effective strategy to detect symmetry of the Fermi surface, hidden phases, and topological phase transitions.[20,21] In general, the AMR originates from the variations in conductivity and the density of states (DOS) at the Fermi level under a magnetic field.[22,23] The symmetry of the AMR is intimately related to the symmetries of the crystal and magnetic sublattice, usually exhibiting two-fold symmetry.[23,24] However, unlike the normal AMR, the anomalous AMR with higher order symmetries can be also observed with the occurrences of the metamagnetic transition, topological transition, or carrier density alteration,[25,26] garnering more and more attention due to the significant physical implications and substantial advantages in applications. Taking advantage of the tunability of spin-frustration-induced magnetism and a combination of topological bands and magnetism, diverse magnetoresistance behaviors, such as the negative magnetoresistance and normal AMR, have been observed in the magnetic kagome materials.[27,28] However, the anomalous AMR is still rarely studied.

Here we report the discovery of an anomalous AMR, the field-induced butterfly-like AMR, in an intriguing kagome semimetal $Co_3In_2S_2$. By using a polycrystal-source chemical vapor transport (PS-CVT) approach, high-quality hexagonal-shaped $Co_3In_2S_2$ single crystals are successfully synthesized, with a high carrier mobility reaching $10^4$ $cm^2V^{-1}s^{-1}$. The magnetic measurements demonstrate that the $Co_3In_2S_2$ single crystal undergoes a canted antiferromagnetic transition at 5 K. However, such antiferromagnetic order can be easily disrupted and transformed into a ferromagnetic order under a small magnetic field. Through the low-temperature magneto-transport measurements, we observe the planar Hall effect (PHE), which originates from the complex contributions of the field-induced ferromagnetism and orbital magnetoresistance. Notably, we observe a field-induced butterfly-like AMR with increasing magnetic field, which exhibits intriguing four- and six-fold symmetries. Density functional theory (DFT) calculations suggest that such a field-induced butterfly-like AMR in the kagome $Co_3In_2S_2$ may originate from the modulations of the electronic structure by the external magnetic field. Our work provides a deep understanding of the interplay between the topological band and magnetism in the kagome systems.

## 2. Synthesis and Structure Characterizations of $Co_3In_2S_2$ Single Crystals

The $Co_3In_2S_2$ is crystallized in a rhombohedral structure with the space group R-3m (No. 166), where the Co atoms form a kagome lattice in the *ab* plane and stack along the *c*-axis (**Figure 1**a). High-quality $Co_3In_2S_2$ single crystals are synthesized by the PS-CVT method, where small polycrystalline granules of $Co_3In_2S_2$ and halide are taken as the vapor source and transport agent (Figure S1, Supporting Information). The synthesized $Co_3In_2S_2$ single crystal shows a regular hexagonal shape with a lateral size of millimeters (Figure 1b), demonstrating a preferential growth of the *ab* plane. The XRD pattern only shows the (00*l*) diffraction peaks and the rocking curve obtained from the (003) reflection reveals a fairly small full-width-half-maximum (FWHM) value of ≈0.08° (Figure 1c). The (*hk*0) plane diffraction pattern of the $Co_3In_2S_2$ crystal shows sharp diffraction spots without splitting (Figure 1d). The crystalline data and structure refinement for the $Co_3In_2S_2$ single crystal are shown in Figure S2 (Supporting Information). The lattice constants *a*, *b*, and *c* are determined to be 5.32 5.32 and 13.68 Å, respectively. These results confirm the pure phase and high quality of the as-grown $Co_3In_2S_2$ single crystals.

To further examine the quality of the as-grown $Co_3In_2S_2$ crystals, we perform atomic-scale structural analysis. The scanning tunneling microscopy (STM) topography shows a perfect hexagonal symmetry and the measured lattice constant is about 5.25 Å (Figure 1e), which is consistent with the results of the single-crystalline diffraction. X-ray energy dispersive spectroscopy (EDS) shows uniform distributions of the Co, In, and S elements with an atomic ratio of Co:In:S close to 3:2:2 (Figure S3a,b, Supporting Information). The high-resolution transmission electron microscopy (HRTEM) images and selected area electron diffraction (SAED) image exhibit a lattice spacing of 0.33 nm, which corresponds to the (012) plane of $Co_3In_2S_2$ (Figure S3c, Supporting Information). Moreover, the aberration-corrected scanning transmission electron microscopy (STEM) images of the $Co_3In_2S_2$ crystals along the [100] zone axis (Figure 1f,g; Figure S4a–h, Supporting Information) further reveal the perfect atomic arrangements without noticeable structural defects.

## 3. Magnetic Properties, Large Magnetoresistance, and High Carrier Mobility

We next study the magnetic properties of the high-quality $Co_3In_2S_2$ single crystal. The temperature-dependent magnetization of the $Co_3In_2S_2$ single crystal shows an antiferromagnetic transition at 5 K ($T_N$ = 5 K) (**Figure 2**a). However, such antiferromagnetic order can be easily broken when the applied external magnetic field increases. Under the field of 0.1 T and 0.3 T, the $Co_3In_2S_2$ single crystal reveals an out-of-plane ferromagnetic order with a saturation magnetization ($M_s$) of 0.07 $\mu B$ per Co atom and a small coercivity of 0.026 T at 2 K (Figure 2b; Figure S5a,b, Supporting Information). Moreover, such a field-induced ferromagnetic order can persist to 100 K (Figure S5c, Supporting Information). We have also measured the field dependence of the magnetization at different rotation angles of 0°, 30°, 45°, 60°, and 90°, showing different magnetization intensities at different angles. Based on these results, we speculate that the $Co_3In_2S_2$ single crystal has a canted antiferromagnetic texture, in which the moments of the Co atoms within the kagome plane stack along the *c*-axis non-collinearly (Figure S5d, Supporting Information).[29,30] Additionally, the sudden jump around 190 K ($T_S$) is possibly related to a magnetic transition from a spiral magnetic structure to a frustrated triangular magnetic structure (Figure S6, Supporting Information), similar to magnetic structure in kagome $Mn_3Sn$.[31]

ADVANCED FUNCTIONAL MATERIALS
www.afm-journal.de

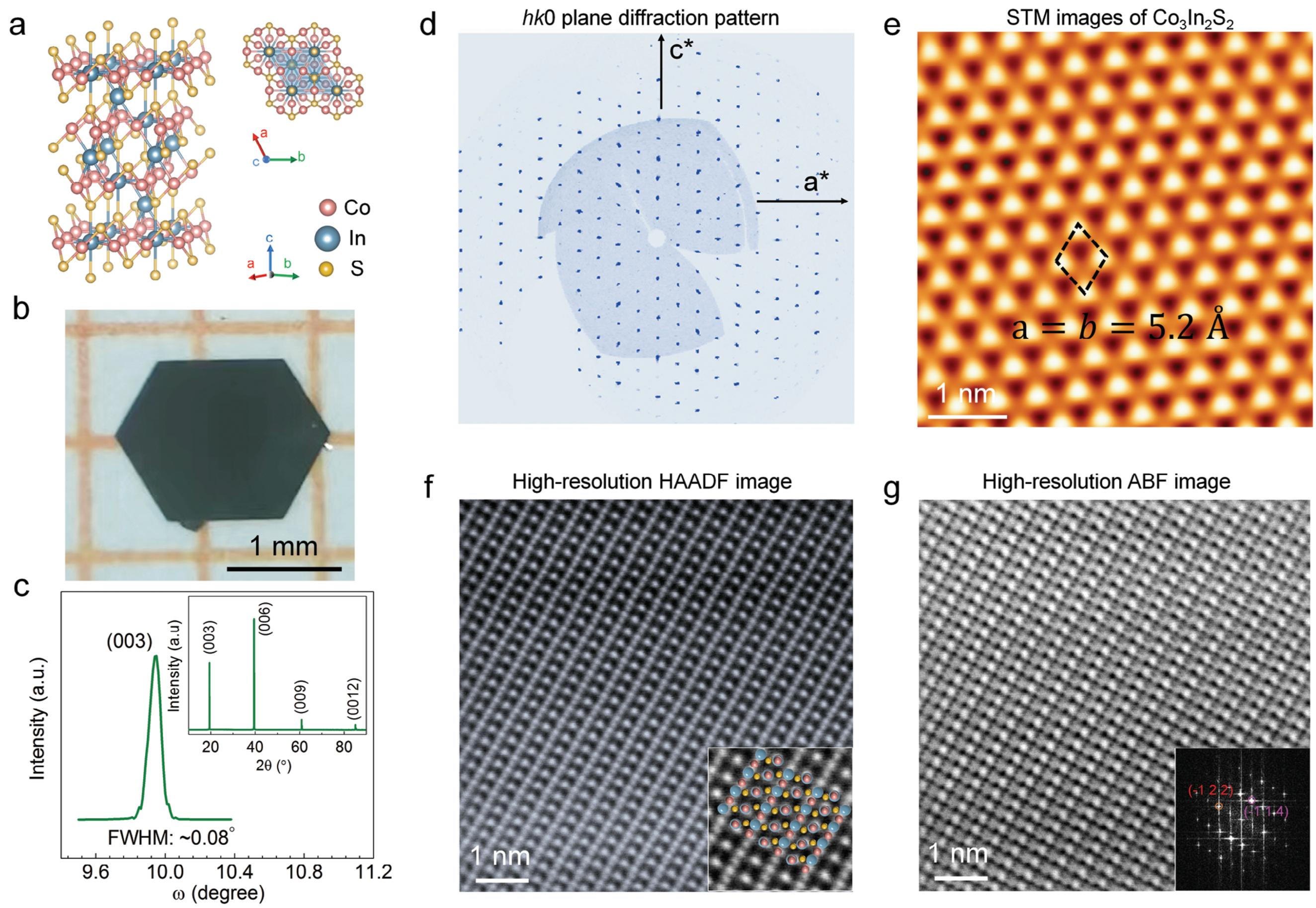


**Figure 1.** Synthesis of high-quality kagome-lattice $Co_3In_2S_2$ single crystals and structural characterizations. a) Schematic of the crystalline structure of the kagome-lattice $Co_3In_2S_2$. The Co atoms form a kagome plane. Pink, blue and yellow balls represent Co, In and S atoms, respectively. b) An optical photograph of the $Co_3In_2S_2$ single crystal synthesized by the PS-CVT method, showing a regular hexagonal shape with a lateral size of about 2 mm. c) The X-ray rocking curve of the (003) reflection of the $Co_3In_2S_2$ crystal, showing a small FWHM of 0.08°. The inset shows X-ray diffraction pattern of the $Co_3In_2S_2$ single crystal. d) The (hk0) plane diffraction patterns of the $Co_3In_2S_2$ crystal, showing sharp diffraction spots without splitting. e) An atomic-resolution STM image taken on a cleaved S surface of the $Co_3In_2S_2$ crystal (5 nm × 5 nm, Scanning bias $U = 300$ mV, current $I = 50$ pA), showing a perfect hexagonal symmetry and lattice constant of 5.25 Å. f) High-resolution HAADF STEM image along the [100] zone axis of the $Co_3In_2S_2$ single crystal. The atomic structure of the $Co_3In_2S_2$ overlays in the inset, agreeing very well with the experimental result. g) The corresponding ABF image of the $Co_3In_2S_2$ crystal. Inset shows the SAED pattern.

Figure 2c shows the temperature-dependent longitudinal resistivity under various magnetic fields of 0, 1, 3, 5, 7 and 9 T, which indicates a metallic nature of $Co_3In_2S_2$. The residual resistivity is 0.069 μΩ cm at 2 K and the residual resistivity ratio (RRR) $\rho_{300K}/\rho_{2K}$ reaches 1600, indicating the low scattering in high-quality $Co_3In_2S_2$ single crystals. Moreover, the resistivity within the temperatures ranging from 2 to 100 K can be well fitted by a relation: $\rho\,(T) = \rho_{xx}\,(0) + bT^n$ (Figure S7a, Supporting Information), where $\rho_{xx}(0)$ is the residual resistivity and $b$ is a predetermined constant factor. The fitting results give an exponent of $n \approx 2.09$, suggesting that the electron–electron interaction is dominant in $Co_3In_2S_2$ at low temperatures. In addition, the MR under the out-of-plane magnetic field exhibits saturation with a maximum value of 480% at 2 K, whereas it gradually turns to be non-saturating with the increase of temperature (Figure 2d). Compared with the large MR under the out-of-plane magnetic fields, $Co_3In_2S_2$ single crystal only shows a positive MR less than 74% under the in-plane fields, indicating a strong out-of-plane anisotropy (Figure 2e). To understand the complex $MR$ phenomena, we perform a power law fitting by using the Kohler rule: $MR = a{\cdot}(m_0H/\rho_0)^n$, where $\rho_0$ is the zero-field resistivity and $a$ and $n$ are the constants (Figure S7, Supporting Information). The fitting results demonstrate the semimetallic characteristic of $Co_3In_2S_2$. Moreover, the crossover from the low-field $B^{n>1}$ dependence to the high-field linear dependence suggests the possible existence of Dirac nodal lines in $Co_3In_2S_2$.[32–34]

Furthermore, the $Co_3In_2S_2$ single crystal exhibits a linear field-dependent Hall resistivity $\rho_{xy}$ from 2 to 80 K in an out-of-plane configuration (Figure S8a, Supporting Information), suggesting that the hole dominates the electrical transport properties. The extremely high Hall conductivity of $10^6$ $\Omega^{-1}$cm$^{-1}$ and longitudinal conductivity of $10^7$ $\Omega^{-1}$cm$^{-1}$ imply that $Co_3In_2S_2$ hosts potential for applications in high-sensitivity sensors (Figure S8b–d, Supporting Information). We extract the carrier concentrations and mobilities at various temperatures by using the single-carrier Drude model (Figure 2f). As the result, the carrier

 

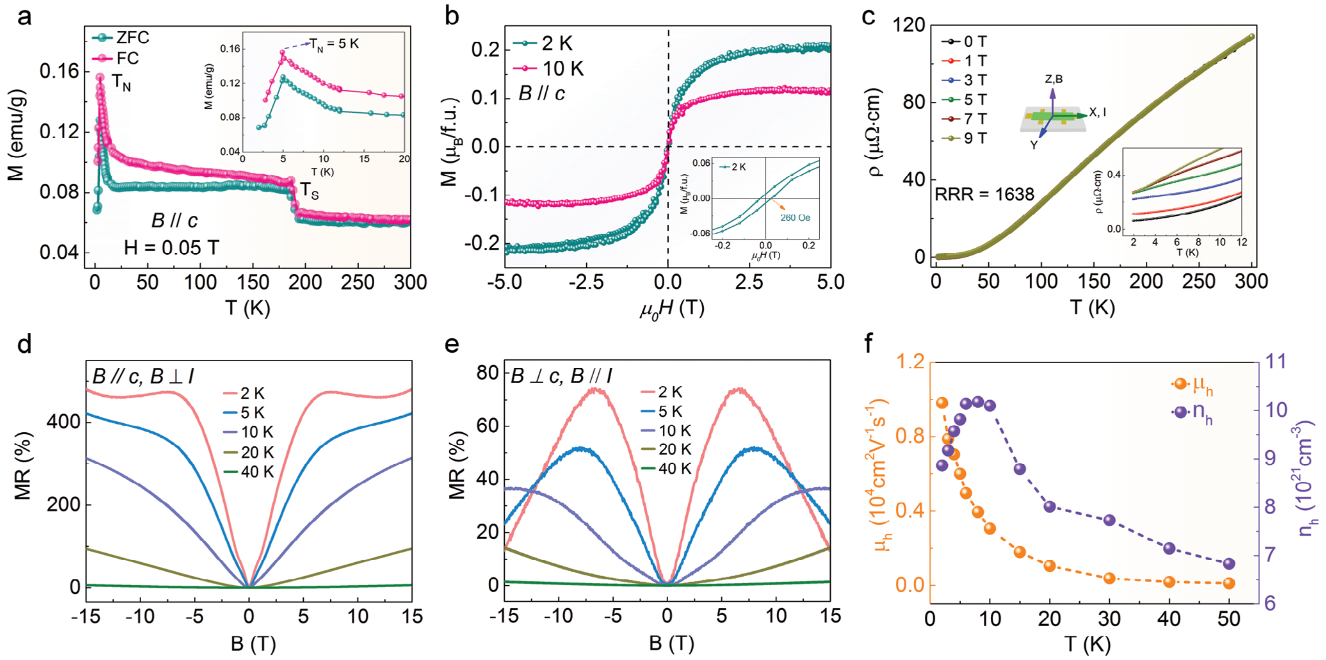


**Figure 2.** Magnetic properties, magnetoresistance and carrier mobility of the $Co_3In_2S_2$ single crystals. a) Temperature dependence of the magnetization of the $Co_3In_2S_2$ single crystals with ZFC and FC procedures under an out-of-plane magnetic field of 0.05 T, showing an antiferromagnetic transition at 5 K. Inset is the enlarged curves, clear showing the magnetic transition. b) Field dependence of the magnetization at 2 and 10 K. The inset shows the enlarged part of the magnetization curve at 2 K, showing a small coercivity of 0.026 T. c) Temperature dependence of the resistivity under various magnetic fields of 0, 1, 3, 5, 7 and 9 T, showing a large RRR of 1638 and small residual resistivity of 0.069 μΩ·cm at 0 T. d) MR measured under the out-of-plane magnetic fields up to 15 T at various temperatures from 2 to 40 K, showing a saturated MR at low temperatures whereas a non-saturated MR at relatively high temperatures. e) MR measured under the in-plane magnetic fields up to 15 T at various temperatures from 2 to 40 K. f) Temperature dependence of the carrier mobility ($\mu_h$) and concentration ($n_h$), showing the mobility of 9810 $cm^{-2}V^{-1}s^{-1}$ at 2 K.

mobility reaches 9810 $cm^2V^{-1}s^{-1}$ at 2 K and the corresponding carrier concentration is $8.8 \times 10^{21}$ $cm^{-3}$. The mobility of $Co_3In_2S_2$ is the larger than most reported magnetic semimetals (Figure S8e, Supporting Information), (e.g., $Co_3Sn_2S_2$ ≈2600 $cm^2V^{-1}s^{-1}$, $MnBi_2Te_4$ ≈3110 $cm^2V^{-1}s^{-1}$, GdPtBi ≈1500 $cm^2V^{-1}s^{-1}$).[35–37]

## 4. In-Plane AMR and Planar Hall Effect

We further study the angle-dependent magneto-transport properties of the $Co_3In_2S_2$ single crystal. **Figure 3a** shows the angular dependence of in-plane AMR measured at 2 K, which reveals two-fold symmetry with a maximum of 35% under 9 T. Besides, the AMR effect weakens monotonically as the temperature increases and persists to 80 K under 5 T (Figure 3b). More importantly, the $Co_3In_2S_2$ single crystal clearly exhibits PHE, as shown Figure 3c,d. The angular dependence of the AMR and planar Hall resistivity can be given by the following expressions,[38–40]

$$\rho_{xy}^{PHE} = -\Delta\rho_{xy} sin\varphi cos\varphi + b \quad (1)$$

$$AMR_{ratio} = \left(\frac{\rho_{xx,\varphi} - \rho_{xx,\perp}}{\rho_{xx,\perp}}\right) \times 100\% \quad (2)$$

$$\rho_{xx} = \rho_{\perp} - \Delta\rho_{xy} cos^2\boldsymbol{\varphi} \quad (3)$$

where $\Delta\rho_{xy} = \rho_{\perp} - \rho_{//}$ refers to the chiral anomaly-induced resistivity, $\rho_{\perp}$ and $\rho_{//}$ are regarded as the longitudinal resistivity when $B$ is perpendicular or parallel to $I$, respectively. The extracted $\Delta\rho_{xy}$ exhibits a power law dependence on the magnetic field with an exponent of 1.32 (Figure 3e; Figure S9a, Supporting Information) and an overall decrease with increasing the temperature to 80 K (Figure 3f; Figure S9b, Supporting Information).

Generally, there are three likely microscopic mechanisms contributing to the PHE, i.e., i) chiral anomaly effect related to chiral charge pumping in Weyl semimetals; ii) anisotropic orbital magnetoresistance, which stems from the anisotropy of Fermi pockets, resulting in $\rho_{\perp} > \rho_{//} > 0$; iii) spin-dependent scattering effects in ferromagnets, arising from the angle between the directions of the magnetization and the current.[38,39] For the chiral anomaly-induced PHE, it requires a negative MR ($B$ // $I$), $B^2$-dependent $\Delta\rho_{xy}$,[41] and decrease of $\rho_{//}$ with increasing $B$.[40] In the case of $Co_3In_2S_2$, there shows a positive $MR$ (Figure 2e). Moreover, the fitted exponent (1.32) for $\Delta\rho_{xy}$ is much less than 2 and both the $\rho_{\perp}$ and $\rho_{//}$ increase with the magnetic field (Figure S9c,d, Supporting Information). These results rule out the chiral anomaly origin for PHE. Additionally, we find $\rho_{\perp} > \rho_{//} > 0$ in the $Co_3In_2S_2$, which agrees with the anisotropic orbital magnetoresistance mechanism. Moreover, the planar Hall resistivity overall reduces as the temperature increases and eventually disappears around 100 K. In the temperature range of PHE, $Co_3In_2S_2$ exhibits a weak field-induced ferromagnetism, suggesting that the origin of PHE is also likely associated with spin-dependent scattering effects. Therefore, we attribute PHE in $Co_3In_2S_2$ to the complex contributions of the spin scattering and orbital $MR$.

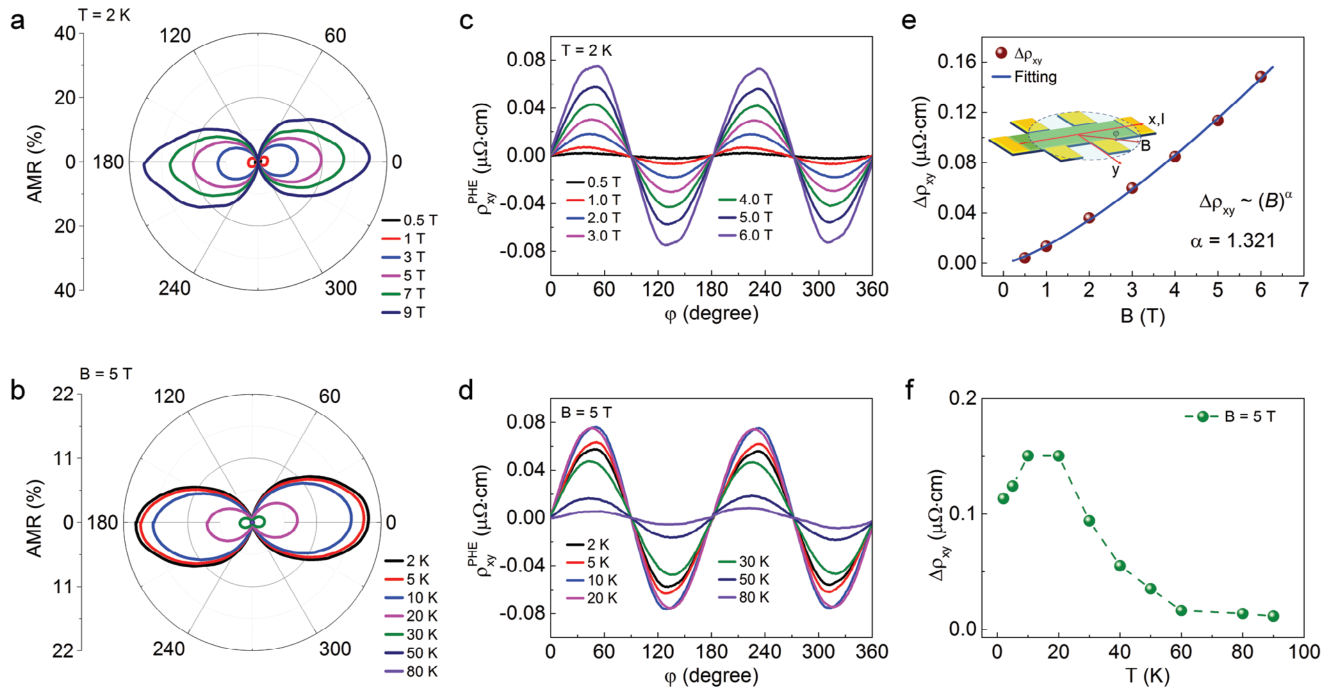


**Figure 3.** In-plane AMR and PHE of the kagome-lattice $Co_3In_2S_2$ single crystal. a) In-plane AMR at 2 K under various magnetic fields of 0.5, 1, 3, 5, 7 and 9 T. b) AMR under 5 T at different temperatures from 2 to 80 K. c) Planar Hall resistivity at 2 K under different magnetic fields of 0.5, 1, 2, 3, 4, 5, and 6 T. d) Planar Hall resistivity under 5 T at temperatures from 2 to 80 K. e) Field dependence of the $\Delta\rho_{xy}$ obtained by fitting the curves in (c), following a power law with an exponent of 1.32. The inset shows a typical PHE measurement setup. The longitudinal and transverse voltages corresponding to the in-plane AMR and planar Hall resistivity are measured with the magnetic field B rotating in the ab-plane. f) Temperature dependence of $\Delta\rho_{xy}$ obtained from fitting in (d).

## 5. Field-Induced Butterfly-Like Anomalous Out-of-Plane AMR

Subsequently, we focus on the study of the out-of-plane *MR* behavior. The *MR* with different angles under magnetic fields rotating along the *z*–*x*-plane displays the diverse field dependence curves, demonstrating a strong and unusual anisotropy characteristic (**Figure** 4a). As the angle increases with an interval of 15°, the *MR* shows a trend of initially increasing and then decreasing with a maximum value of 1100% at $\theta = 45°$ and a non-saturated linear behavior at $\theta = 45°$ and 60°. To further investigate the angular dependence of the out-of-plane AMR, we perform comprehensive characterizations at a series of magnetic fields and temperatures. The AMR at 2 and 5 K under different magnetic fields is illustrated in Figure 4b–f, which distinctly show that the AMR exhibits a dramatic change. Under $B < 1$ T, the AMR of the $Co_3In_2S_2$ single crystal reveals the conventional two-fold symmetry (Figure 4b). As $B$ increases to 3 T, the amplitude of the peaks at 0° and 180° obviously enhances. As $B$ continually increases, the intensity of signals at 0° and 180° somewhat weakens, whereas the signals around 45°, 135°, 225°, and 315° become dominant and gradually split into two sharp peaks. Up to high magnetic fields, this double-peak feature is stable and the AMR curve exhibits an unconventional butterfly shape. During this process, the amplitude of the AMR shows a giant anisotropy value of 850% at 2 K under 9 T (Figure 4f).

The field-induced anomalous butterfly-like AMR indicates the conventional two-fold symmetry is broken, that is, the AMR components with four- and six-fold symmetries appear under the high magnetic fields. The butterfly-like AMR is the superposition of the two-, four-, and six-fold AMR terms. As shown in the 3D planform of the AMR (2 K, 0.5-9 T), it can be clearly found that the four- and six-fold AMR appear above 2 T and persist to 9 T (Figure 4g). Moreover, from the temperature-dependent AMR (Figure 4h; Figure S10, Supporting Information), the higher-order AMR signals will gradually disappear with increasing temperature and the normal two-fold AMR dominates at high temperatures. Under $B = 9$ T, the six-fold AMR can be distinguished even at temperatures up to 20 K, whereas the critical temperature lowers to about 10 K under 5 T. Figures S11 and S12 (Supporting Information) show the 3D planform of the AMR effect at $T = 3$, 5, 8, 10 K under $0.5\ \mathrm{T} \le B \le 9$ T, where the sixfold symmetry of AMR manifests in diverse butterfly shapes that gradually weaken as the temperature increases.

To further understand the anomalous AMR behaviors, we employ symmetry considerations to calculate the AMR components:[42]

$$AMR = C_0 + C_2 cos^2\theta + C_4 cos^4\theta + C_6 cos^6\theta \tag{4}$$

where $C_0$ is a constant, $C_2 cos^2\theta$, $C_4 cos^4\theta$ and $C_6 cos^6\theta$ account for the two-, four-, and six-fold components, respectively. From the details of the fitting as shown in Figure S13 (Supporting Information), the amplitudes of the $C_2$, $C_4$ and $C_6$ at different temperatures and magnetic fields can be obtained, which correspond to the three components of AMR. The extracted $C_2$, $C_4$, and $C_6$ at 2 K

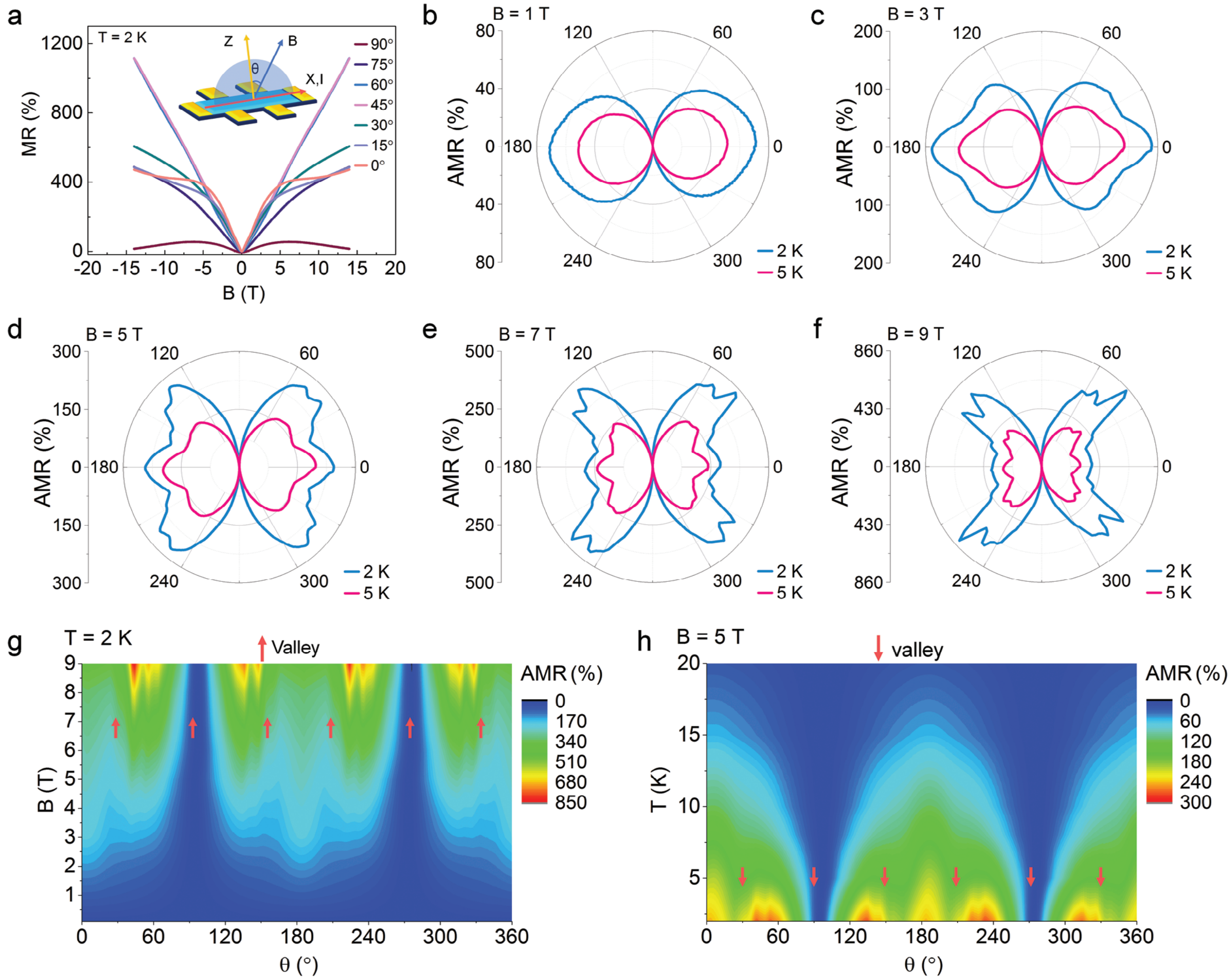


**Figure 4.** Field-induced butterfly-like out-of-plane AMR of the $Co_3In_2S_2$ single crystal. a) Magnetic field dependence of *MR* at 2 K with different magnetic field orientations $\theta_{zx}$. The inset shows the schematic of the measurement configuration, where the magnetic field rotates in the *z*–*x*-plane. b–f) AMR at 2 K and 5 K under the different magnetic fields of 1, 3, 5, 7, and 9 T. g) The 3D planform of AMR for T = 2 K and 0.1 T < B < 9 T. h) The 3D planform of AMR for B = 5 T and 2 < T < 20 K. The color contrast indicates the change of resistivity.

as the function of *B* are shown in Figure S14a–c (Supporting Information). As a result, the proportion of the $C_2$ signal decreases rapidly from 62% to 26% as the magnetic field increases to 2 T, whereas the proportions of the $C_4$ and $C_6$ signals increase dramatically. With continuously increasing *B*, the $C_4$ almost remains constant while the $C_6$ gradually reduces. Moreover, the proportion of the $C_4$ signal (about 50%) is larger than that of both the $C_2$ and $C_6$ signals. To further analyze the temperature dependence, we extracted the $C_2$, $C_4$, and $C_6$ values at various temperatures ranging from 2 K to 50 K under a magnetic field of 9 T (Figure S14d–f, Supporting Information). As the temperature increases from 2 to 50 K, the proportion of the $C_2$ signal rapidly rises from 26% to 93%, while the proportions of the $C_4$ and $C_6$ signals gradually decrease and nearly disappear around 50 K, indicating that the two-fold AMR dominates at high temperatures.

Additionally, we have observed that several small splitting peaks on the AMR gradually disappeared under the same external field as the temperature increased (Figure 4d–f), which indicates that the influence of the Lorentz force is weak. Furthermore, we have also performed AMR measurements under the applied magnetic field always perpendicular to the current (as illustrated in Figure S15a, Supporting Information). The field-induced butterfly-like AMR effect has also been observed (Figure S15b–f, Supporting Information) and the proportions of the two-, four-, and six-fold signals (Figures S16 and S17, Supporting Information) are similar to the results observed in the configuration with the magnetic field rotation direction in the *z*–*x*-plane. These results demonstrate that the Lorentz force has a negligible influence on the field-induced butterfly-like AMR effect.

The anomalous AMR with high-order symmetries usually originates from the magnetocrystalline anisotropy,[43] spin-dependent scattering near antiphase boundaries (APBs),[44] or modulation of the DOS near the Fermi surface.[23,24] In general, if the magnetic field is strong enough to overcome the magnetic

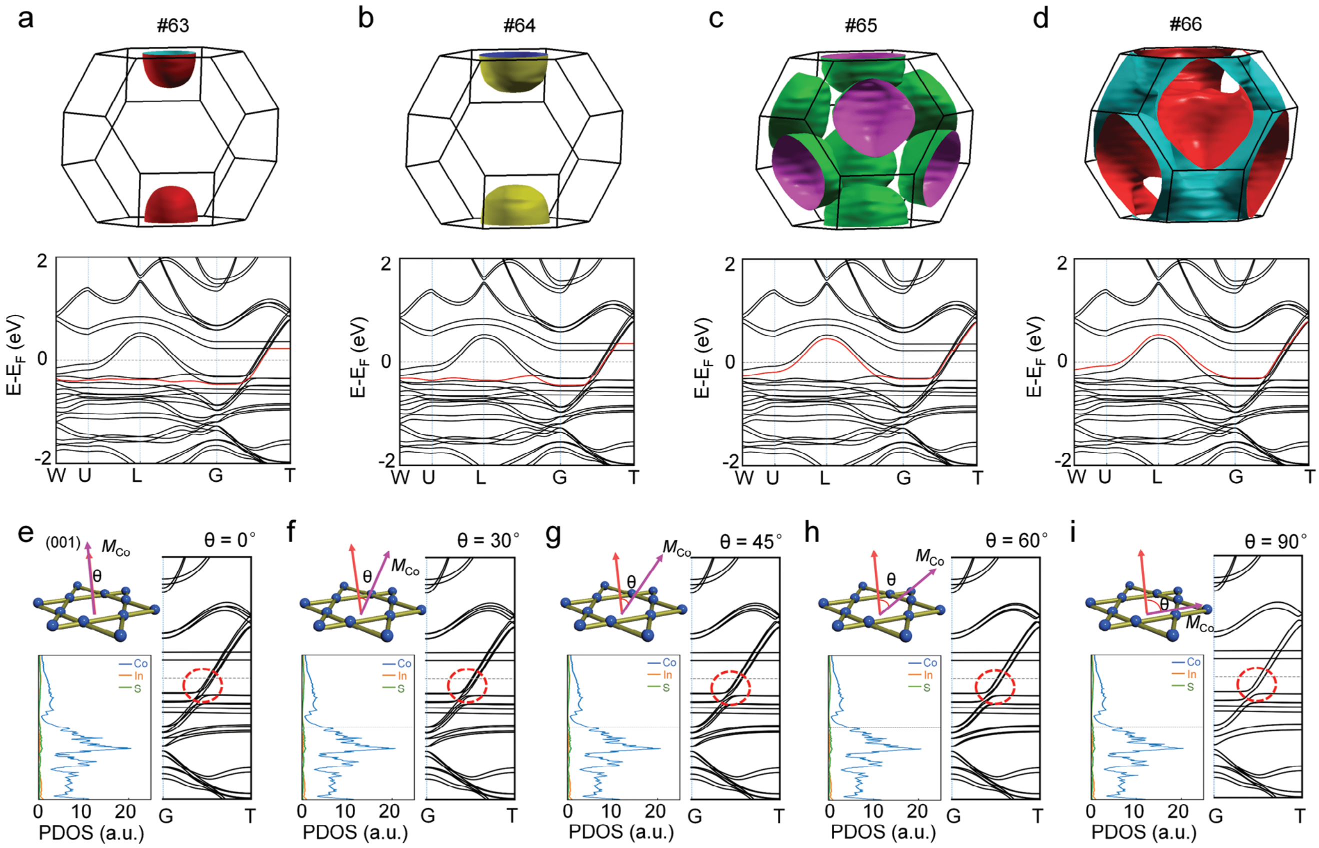

**Figure 5.** Calculated Fermi surfaces and density of states for the kagome-lattice $Co_3In_2S_2$ single crystal. a–d) Band structures with four bands crossing the Fermi level (lower panels) and the corresponding Fermi surfaces (upper panels) for the four bands. The four bands are labeled as 63, 64, 65, 66, and highlighted by the red curves. The bands 63 and 64 exhibit Fermi surfaces with a two-fold symmetry, while bands 65 and 66 show Fermi surfaces with a six-fold symmetry. e–i) The calculated band structures (with SOC) along the Γ–T direction of the $Co_3In_2S_2$ with the magnetic moments of the Co atoms rotating in the *z*–*x*-plane. As the magnetic moment rotates from 0° to 90°, the four bands undergo a transition from a non-degenerate to degenerate state, resulting in band crossings and structural reconstructions. The red circles highlight the evolution of band structure splitting near the Fermi level.

anisotropy field, the high-order AMR will be suppressed.[45] In the case of $Co_3In_2S_2$ single crystals, both four- and six-fold AMR can persist even to 9 T, thus we rule out the magnetocrystalline anisotropy mechanism. Additionally, high-order AMR resulting from the APBs mechanism can only be observed under in-plane magnetic fields rather than the out-of-plane configuration.[39,46] Therefore, we speculate that the field-induced anomalous AMR effect possibly arises from the modulations of the DOS near the Fermi level of the $Co_3In_2S_2$ by the external magnetic fields.

## 6. Origin of the Field-Induced Butterfly-Like AMR

To gain a deeper insight into the field-induced butterfly-like AMR effect in the kagome-lattice $Co_3In_2S_2$, we calculate the Fermi surface and density of states of $Co_3In_2S_2$ based on DFT. **Figure** 5a-d provides the band structures with the four bands crossing the Fermi level and the corresponding Fermi surfaces in the first Brillouin zone. The four bands are labeled as 63, 64, 65, and 66, and highlighted by red curves. Based on the relationship between the symmetry of the AMR signal and the Fermi surface, the symmetry of the AMR agrees with that of the Fermi surface. The Fermi surfaces of the bands 63 and 64 exhibit a two-fold symmetry, which may be related to the $C_2$ signal. While bands 65 and 66 form the Fermi surfaces with a six-fold symmetry, which could contribute to the $C_6$ signal. Moreover, according to the projected band structures of the Co 3d orbitals, the $d_{xy}$ and $d_{z^2}$ orbitals of the four bands exhibit a cloverleaf and a dumbbell shape with a central ring, respectively (Figure S18, Supporting Information). The transport properties can be influenced by the distribution of the surrounding electronic states and the orbital symmetries. Thus, under the external magnetic fields, the directional dependence due to the symmetry of *d*-electron orbitals may result in a four-fold AMR effect.[47,48]

Due to the spatially canted antiferromagnetic structure of $Co_3In_2S_2$, it is expected that the magnetic moments of the cobalt atoms would rotate in the *z*–*x*-plane along the external magnetic field. To uncover the field dependence of the butterfly-like AMR, we further study the evolution of band structures of the $Co_3In_2S_2$ as the magnetic moments of Co atoms rotate in the *z*–*x*-plane (Figure 5e–i). With the moments rotating from 0° to 90°, the band structure along the Γ–T direction alters from a splitting state to a degenerate state, leading to the band crossings and structural reconstructions, which changes DOS near the Fermi level and further affects the scattering probability of the conduction electrons in different directions, thereby inducing the anomalous four- and six-fold AMR.

In summary, we have successfully synthesized an intriguing kagome semimetal $Co_3In_2S_2$ single crystals by using a modified CVT approach. The high-quality, hexagonal-shaped $Co_3In_2S_2$ single crystal exhibits a high carrier mobility of $10^4$ $cm^2V^{-1}s^{-1}$ and a giant AMR of 850%. Besides, the $Co_3In_2S_2$ single crystal has a spatially canted antiferromagnetic structure below 5 K. Due to the magnetic tunability under the external magnetic field, the PHE and an anomalous butterfly-like AMR effect are clearly observed in the kagome-lattice $Co_3In_2S_2$. Such butterfly-like AMR exhibits the superposition of the two-, four-, and six-fold symmetries. Combining the band structure calculations, we attribute the field-induced anomalous AMR to the modulations of the electronic structure of the Fermi level of the $Co_3In_2S_2$ by the external magnetic fields. Our study provides a deep understanding of the anomalous AMR phenomenon. The kagome semimetal $Co_3In_2S_2$ with a giant AMR presents rich physics, holding promise for practical applications in electronic and spintronic devices.

## 7. Experimental Section

*Synthesis of the Kagome-Lattice $Co_3In_2S_2$ Single Crystals*: The kagome-lattice $Co_3In_2S_2$ single crystals were successfully synthesized by a chemical vapor transport approach using the polycrystalline $Co_3In_2S_2$ granules as the source materials. First, $Co_3In_2S_2$ polycrystals with irregular shapes were prepared by the self-flux method, in which the raw materials of Co, In, and S were mixed in a molar ratio of Co:In:S = 3:2:2 and placed in a crucible, then sealed in a quartz tube using a high temperature flame gun under high vacuum. The quartz tube was slowly heated for 55 h to 1050°C, then kept constant at that temperature for 24 h and then cooled to 600 °C at a rate of 10 °C $h^{-1}$. Subsequently, the growth of the hexagonal-shaped $Co_3In_2S_2$ single crystals were performed in a temperature gradient from 1000 to 900 °C for about a week, with the polycrystal granules as the vapor sources and $NH_4Cl$ as the transport agent.

*Sample Characterizations*: XRD patterns were taken by a Rigaku SmartLab SE X-ray diffractometer with Cu K$\alpha$ radiation ($\lambda$ = 0.15418 nm) at room temperature. A Bruker D8 VentureSingle was adopted for obtaining crystal diffraction patterns and rocking curves. Scanning electron microscopy (SEM) and X-ray energy-dispersive spectroscopy (EDS) were performed using a HITACHI S5000 with an energy dispersive analysis system Bruker XFlash 6|60. STM measurements were performed on a combined nc-AFM/STM system in a Createc system with a base pressure lower than $2 \times 10^{-10}$ bar at 4.5 K. Magnetization measurements were carried out on single crystals with the magnetic field applied along *z* axis by a vibrating sample magnetometer (MPMS 3, Quantum Design). Electrical transport measurements were collected on a Quantum Design Physical Properties Measurement System (PPMS).

*DFT Calculations*: First-principles calculations are performed in the framework of density functional theory (DFT), as implemented in the Vienna Ab Initio Simulation Package (VASP).[49] The projected-augmented-wave (PAW) pseudopotentials were applied to describe the electron–ion interaction with a plane-wave cutoff of 400 eV.[50] Here, Co-$4s^23d^7$, In-$4d^{10}5s^25p$ and S-$3s^23p^4$ electron states were treated as valence electrons. The Perdew–Burke–Ernzerhof (PBE) functional was used to deal with the electron exchange-correlation potentials.[51] The primitive cell of $Co_3In_2S_2$ was considered in our calculations, and a $10 \times 10 \times 10$ k-point grid is applied. The atomic position and lattice parameters were fully relaxed until the residual force on each atom is less than 0.01 eV Å$^{-1}$.

## Supporting Information

Supporting Information is available from the Wiley Online Library or from the author.

## Acknowledgements

The work was supported by grants from the National Key Research and Development Projects of China (2022YFA1204100, 2023YFB3809200), the National Natural Science Foundation of China (62488201), the Chinese Academy of Sciences (XDB33030100, ZDBS-SSW-WHC001, YSBR-003, YSBR-053). The Innovation Program of Quantum Science and Technology (2021ZD0302700).

## Conflict of Interest

The authors declare no conflict of interest.

## Author Contributions

H.T.Y. and H.-J.G. designed the project. S.H.L. and H.G. prepared the samples. S.H.L. and J.H. performed the magnetization measurements. Q.Z. and L.H. performed the STM experiments. S.X.D., J.B.P., Y.H.L., and N.S. performed the DFT calculations. S.H.L., H.G., L.H.B., Q.Q., G.J.H., R.W.W., K.Z., Z.Z., Y.C.H., W.Q.Y., G.Y.X., and X.L. performed the transport experiments. All authors participated in the data analysis and manuscript writing.

## Data Availability Statement

The data that support the findings of this study are available from the corresponding author upon reasonable request.

## Keywords

butterfly-like AMR effect, canted antiferromagnetic state, high carrier mobility, kagome-lattice $Co_3In_2S_2$, planar Hall effect

Received: July 18, 2024
Revised: August 20, 2024
Published online:

[1] L. D. Ye, M. G. Kang, J. W. Liu, F. von Cube, C. R. Wicker, T. Suzuki, C. Jozwiak, A. Bostwick, E. Rotenberg, D. C. Bell, L. Fu, R. Comin, J. G. Checkelsky, *Nature* **2018**, *555*, 638.
[2] J. X. Yin, W. L. Ma, T. A. Cochran, X. T. Xu, S. S. Zhang, H. J. Tien, N. Shumiya, G. M. Cheng, K. Jiang, B. Lian, Z. D. Song, G. Q. Chang, I. Belopolski, D. Multer, M. Litskevich, Z. J. Cheng, X. P. Yang, B. Swidler, H. B. Zhou, H. Lin, T. Neupert, Z. Q. Wang, N. Yao, T. R. Chang, S. Jia, M. Z. Hasan, *Nature* **2020**, *583*, 533.
[3] A. Bose, A. Haldar, E. S. Sorensen, A. Paramekanti, *Phys. Rev. B* **2023**,*107*, L020411.
[4] B. R. Ortiz, S. M. L. Teicher, Y. Hu, J. L. Zuo, P. M. Sarte, E. C. Schueller, A. M. M. Abeykoon, M. J. Krogstad, S. Rosenkranz, R. Osborn, R. Seshadri, L. Balents, J. F. He, S. D. Wilson, *Phys. Rev. Lett.* **2020**, *125*, 247002.
[5] G. Semeghini, H. Levine, A. Keesling, S. Ebadi, T. T. Wang, D. Bluvstein, R. Verresen, H. Pichler, M. Kalinowski, R. Samajdar, A. Omran, S. Sachdev, A. Vishwanath, M. Greiner, V. Vuleti?, M. D. Lukin, *Science* **2021**, *374*, 1242.
[6] Z. P. Hou, W. J. Ren, B. Ding, G. Z. Xu, Y. Wang, B. Yang, Q. Zhang, Y. Zhang, E. K. Liu, F. Xu, W. H. Wang, G. H. Wu, X. X. Zhang, B. G. Shen, Z. D. Zhang, *Adv. Mater.* **2017**, *29*, 1701144.
[7] S. M. Huang, S. Y. Xu, I. Belopolski, C. C. Lee, G. Q. Chang, B. K. Wang, N. Alidoust, G. Bian, M. Neupane, C. L. Zhang, S. Jia, A. Bansil, H. Lin, M. Z. Hasan, *Nat. Commun.* **2015**, *6*, 7373.

[8] X. Y. Li, W. X. Ji, P. J. Wang, C. W. Zhang, *Nanoscale Adv* **2021**, *3*, 847.
[9] E. K. Liu, Y. Sun, N. Kumar, L. Muechler, A. Sun, L. Jiao, S. Y. Yang, D. Liu, A. J. Liang, Q. N. Xu, J. Kroder, V. Süß, H. Borrmann, C. Shekhar, Z. S. Wang, C. Y. Xi, W. H. Wang, W. Schnelle, S. Wirth, Y. L. Chen, S. T. B. Goennenwein, C. Felser, *Nat. Phys.* **2018**, *14*, 1125.
[10] H. Zhang, C. Q. Xu, X. Ke, *Phys. Rev. B* **2021**, *103*, L201101.
[11] Y. C. Wang, X. F. Zhang, F. Pollmann, M. Cheng, Z. Y. Meng, *Phys. Rev. Lett.* **2018**, *121*, 057202.
[12] L. Muechler, E. K. Liu, J. Gayles, Q. N. Xu, C. Felser, Y. Sun, *Phys. Rev. B* **2020**, *101*, 115106.
[13] M. Li, Q. Wang, G. W. Wang, Z. H. Yuan, W. H. Song, R. Lou, Z. T. Liu, Y. B. Huang, Z. H. Liu, H. C. Lei, Z. P. Yin, S. C. Wang, *Nat. Commun.* **2021**, *12*, 3129.
[14] Y. Q. Xing, J. L. Shen, H. Chen, L. Huang, Y. X. Gao, Q. Zheng, Y. Y. Zhang, G. Li, B. Hu, G. J. Qian, L. Cao, X. L. Zhang, P. Fan, R. S. Ma, Q. Wang, Q. W. i Yin, H. C. Lei, W. Ji, S. X. Du, H. T. Yang, W. H. Wang, C. M. Shen, X. Lin, E. K. Liu, B. G. Shen, Z. Q. Wang, H. J. Gao, *Nat. Commun.* **2020**, *11*, 5613.
[15] S. Nakatsuji, N. Kiyohara, T. Higo, *Nature* **2015**, *527*, 212.
[16] H. J. Liao, Z. Y. Xie, J. Chen, Z. Y. Liu, H. D. Xie, R. Z. Huang, B. Normand, T. Xiang, *Phys. Rev. Lett.* **2017**, *118*, 137202.
[17] P. K. Rout, P. V. P. Madduri, S. K. Manna, A. K. Nayak, *Phys. Rev. B* **2019**, *99*, 094430.
[18] Z. L. Sun, A. F. Wang, H. M. Mu, Z. F. Wang, T. Wu, Z. Y. Wang, X. Y. Zhou, X. H. Chen, *Npj Quantum Mater.* **2021**, *6*, 94.
[19] H. W. Wang, C. L. Lu, J. Chen, Y. Liu, S. L. Yuan, S. W. Cheong, S. Dong, J. M. Liu, *Nat. Commun.* **2019**, *10*, 2280.
[20] M. N. Ali, L. M. Schoop, C. Garg, J. M. Lippmann, E. Lara, B. Lotsch, S. S. P. Parkin, *Sci. Adv.* **2016**, *2*, 1601742.
[21] Y. J. Jo, J. Park, G. Lee, M. J. Eom, E. S. Choi, J. H. Shim, W. Kang, J. S. Kim, *Phys. Rev. Lett.* **2014**, *113*, 156602.
[22] J. J. Wang, J. Deng, X. W. Liang, G. Y. Gao, T. P. Ying, S. J. Tian, H. C. Lei, Y. P. Song, X. Chen, J. G. Guo, X. L. Chen, *Phys. Rev. Mater.* **2021**, *5*, L091401.
[23] Y. Dai, Y. W. Zhao, L. Ma, M. Tang, X. P. Qiu, Y. Liu, Z. Yuan, S. M. Zhou, *Phys. Rev. Lett.* **2022**, *128*, 247202.
[24] J. Chen, H. Li, T. Y. Guo, P. Chen, D. F. Zheng, G. Q. Yu, Y. C. Lau, X. K. Xi, W. H. Wang, *NPG Asia Mater.* **2023**, *15*, 34.
[25] H. Hodovanets, C. J. Eckberg, D. J. Campbell, Y. Eo, P. Y. Zavalij, P. Piccoli, T. Metz, H. Kim, J. S. Higgins, J. Paglione, *Phys. Rev. B* **2022**, *106*, 235102.
[26] J. Xu, F. C. Wu, J. K. Bao, F. Han, Z. L. Xiao, I. Martin, Y. Y. Lyu, Y. L. Wang, D. Y. Chung, M. D. Li, W. Zhang, J. E. Pearson, J. S. Jiang, M. G. Kanatzidis, W. K. Kwok, *Nat. Commun.* **2019**, *10*, 2875.
[27] V. Sharma, R. Nepal, R. C. Budhani, *Phys. Rev. B* **2023**, *108*, 144435.
[28] A. Low, T. K. Bhowmik, S. Ghosh, S. Thirupathaiah, *Phys. Rev. B* **2024**, *109*, 195104.
[29] M. A. McGuire, Q. Zhang, H. Miao, W. Luo, M. Yoon, Y. H. Liu, T. Yilmaz, E. Vescovo, *Chem. Mater.* **2021**, *33*, 9741.
[30] S. Akatsuka, S. Esser, S. Okumura, R. Yambe, R. Yamada, M. M. Hirschmann, S. Aji, J. S. White, S. Gao, Y. Onuki, T. H. Arima, T. Nakajima, M. Hirschberger, *Nat. Commun.* **2024**, *15*, 4291.
[31] N. H. Sung, F. Ronning, J. D. Thompson, E. D. Bauer, *Appl. Phys. Lett.* **2018**, *112*, 132406.
[32] F. Gao, J. Q. Huang, W. J. Ren, M. Z. Li, H. Wang, T. Yang, B. Li, Z. D. Zhang, *Phys. Rev. B* **2022**, *105*, 214434.
[33] W. J. Ren, A. F. Wang, D. Graf, Y. Liu, Z. D. Zhang, W. G. Yin, C. Petrovic, *Phys. Rev. B* **2018**, *97*, 035147.
[34] J. Y. Liu, P. F. Liu, K. Gordon, E. Emmanouilidou, J. Xing, D. Graf, B. C. Chakoumakos, Y. Wu, H. B. Cao, D. Dessau, Q. H. Liu, N. Ni, *Phys. Rev. B* **2019**, *100*, 195123.
[35] M. Tanaka, Y. Fujishiro, M. Mogi, Y. Kaneko, T. Yokosawa, N. Kanazawa, S. Minami, T. Koretsune, R. Arita, S. Tarucha, M. Yamamoto, Y. Tokura, *Nano Lett.* **2020**, *20*, 7476.
[36] C. Liu, Y. C. Wang, M. Yang, J. H. Mao, H. Li, Y. X. Li, J. H. Li, H. P. Zhu, J. F. Wang, L. Li, Y. Wu, Y. Xu, J. S. Zhang, Y. Y. Wang, *Nat. Commun.* **2021**, *12*, 4647.
[37] M. Hirschberger, S. Kushwaha, Z. J. Wang, Q. Gibson, S. H. Liang, C. A. Belvin, B. A. Bernevig, R. J. Cava, N. P. Ong, *Nat. Mater.* **2016**, *15*, 1161.
[38] S. Y. Yang, J. Noky, J. Gayles, F. K. Dejene, Y. Sun, M. Dörr, Y. Skourski, C. Felser, M. N. Ali, E. K. Liu, S. S. P. Parkin, *Nano Lett.* **2020**, *20*, 7860.
[39] X. Ma, M. Huang, S. S. Wang, P. Liu, Y. Zhang, Y. L. Lu, B. Xiang, *ACS Appl. Electron. Mater.* **2023**, *5*, 2838.
[40] Q. Q. Liu, F. C. Fei, B. Chen, X. Y. Bo, B. Y. Wei, S. Zhang, M. H. Zhang, F. J. Xie, M. Naveed, X. Wan, F. Q. Song, B. G. Wang, *Phys. Rev. B* **2019**, *99*, 155119.
[41] S. Nandy, G. Sharma, A. Taraphder, S. Tewari, *Phys. Rev. Lett.* **2017**, *119*, 176804.
[42] Z. Li, W. B. Mi, X. C. Wang, X. X. Zhang, *ACS Appl. Mater. Interfaces* **2015**, *7*, 3840.
[43] J. Li, S. L. Li, Z. W. Wu, S. Li, H. F. Chu, J. Wang, Y. Zhang, H. Y. Tian, D. N. Zheng, *J. Phys.: Condens. Matter* **2010**, *22*, 146006.
[44] P. Li, C. Jin, E. Y. Jiang, H. L. Bai, *J. Appl. Phys.* **2010**, *108*, 093921.
[45] C. R. Hu, J. Zhu, G. Chen, J. X. Li, Y. Z. Wu, *Phys. Lett. A* **2012**, *376*, 3317.
[46] G. L. Zheng, X. D. Zhu, Y. Q. Liu, J. W. Lu, W. Ning, H. W. Zhang, W. S. Gao, Y. Y. Han, J. Y. Yang, H. F. Du, K. Yang, Y. H. Zhang, M. L. Tian, *Phys. Rev. B* **2017**, *96*, 121401(R).
[47] H. W. Ko, H. J. Park, G. Go, J. H. Oh, K. W. Kim, K. J. Lee, *Phys. Rev. B* **2020**, *101*, 184413.
[48] D. Z. Li, F. Pauly, A. Smogunov, *Phys. Rev. Res.* **2020**, *2*, 033184.
[49] G. Kresse, J. Furthmuller, *Comp. Mater. Sci.* **1996**, *6*, 15.
[50] P. E. Blochl, *Phys. Rev. B* **1994**, *50*, 17953.
[51] J. Paier, R. Hirschl, M. Marsman, G. Kresse, *J. Chem. Phys.* **2005**, *122*, 234102.